

Tailoring the Oxygen Evolution Activity and Stability Using Defect Chemistry

Julius Scholz ¹, Marcel Risch ¹, Garlef Wartner ^{1,†}, Christoph Luderer ¹, Vladimir Roddatis ¹ and Christian Jooss ^{1,*}

¹ Institute of Materials Physics, University of Goettingen, Friedrich-Hund Platz 1, 37077 Goettingen; jscholz@ump.gwdg.de (J.S.), mrisch@ump.gwdg.de (M.R.), gwartner@ump.gwdg.de (G.W.), cluderer@ump.gwdg.de (C.L.), vroddatis@ump.gwdg.de (V.R.)

† Current address: Division of Fuel Cells, NEXT Energy, EWE-Forschungszentrum für Energietechnologie, e.V., Carl-von-Ossietzky-Straße 15, 26129 Oldenburg, Germany

* Correspondence: jooss@ump.gwdg.de, Tel.: +49-551-39-5303

Supporting Figures:

- **Figures S1–S2**—XRD analysis
- **Figure S3**—AFM image of LSMO with Mn excess
- **Figures S4–S5**—TEM and EDX analysis on Mn₃O₄ precipitates
- **Figures S6–S7**—SEM evaluation Mn₃O₄ precipitates including the effects of electrochemical treatment
- **Figure S8**—Calibration data for EELS analysis
- **Figures S9–S11**—TEM analysis on Mn valence and O k-edge structure
- **Figure S12**—Gradient analysis for sputtering deposition
- **Figures S13–S14**—Structural and electrochemical effects of Mn off stoichiometry
- **Figure S15**—Ring calibration data
- **Figures S16–S19**—Additional CV and CA measurements for all samples
- **Figure S20**—XRD post-mortem analysis
- **Figure S21**—Effect of strain on activity
- **Figure S22**—Impedance spectroscopy

Supporting Tables:

- **Table S1**—AFM analysis
- **Table S2**—XRR post-mortem analysis
- **Table S3**—OER activities of select perovskite oxides

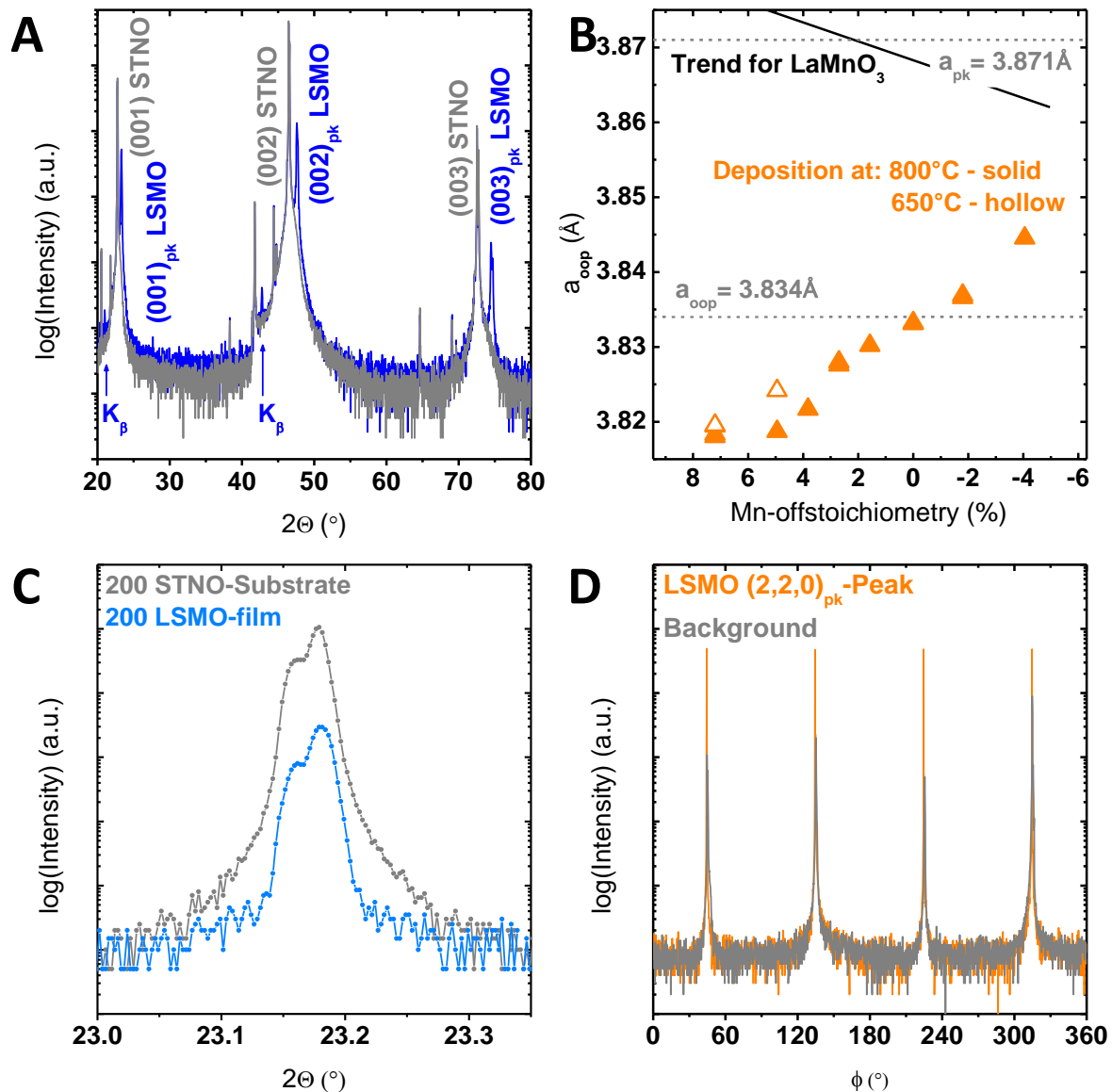


Figure S1. (A) Wide angle 2θ XRD scan on Mn-rich LSMO overlaid by wide angle 2θ XRD scan on Nb:STO substrate; (B) calculated lattice constants of LSMO films with respect to the bulk value; (C) rocking curves on both the Nb:STO substrate reflex and the LSMO reflex of the same sample as presented in (D); (D) ϕ -scan with Ψ at 45° on a typical LSMO film.

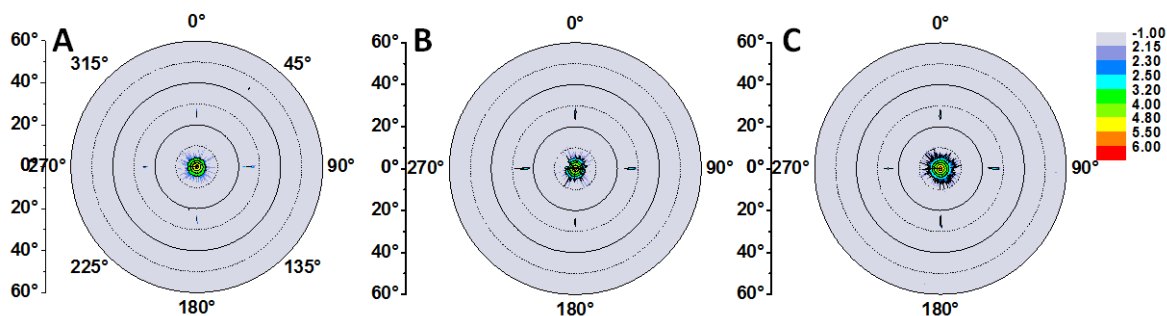


Figure S2. Pole figures of all investigated stoichiometries: (A) Mn deficient; (B) stoichiometric; (C) Mn-rich deposited. Note the logarithmic scale is identical for all pole figures.

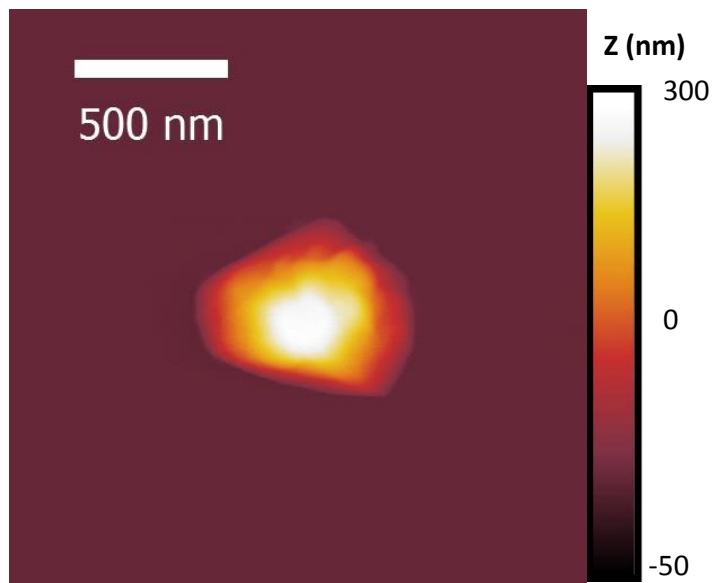


Figure S3. AFM image of LSMO with Mn excess showing a Mn_3O_4 precipitate presented in Figure 1B with a different height scale. Note the chosen height scale here resolves the full height of the Mn_3O_4 precipitate.

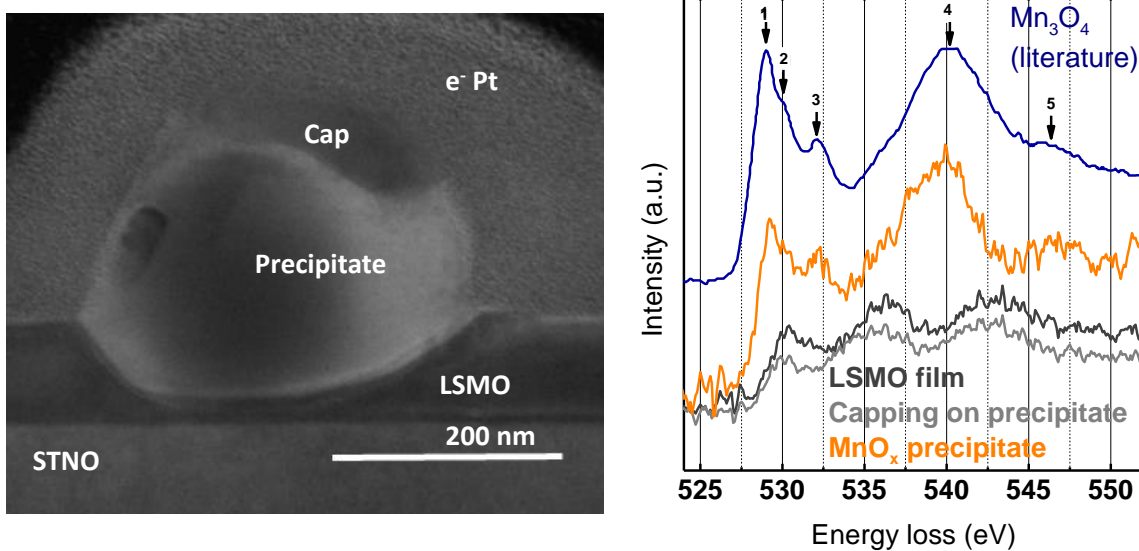


Figure S4. Bright field TEM image a LSMO film with a typical precipitate embedded taken with an acceleration voltage of 120 keV. Indicated are the STNO substrate, the LSMO film, the precipitate and the used protective layer of electron deposited Pt. On top of the precipitate, an additional capping can be seen. O K-edge EELS scans on the LSMO film and the capping suggest that the additional layer consists of LSMO. The comparison of the O K-edge of the precipitate with data from literature in Mn_3O_4 shows similar features (indicated by 1–5) that are only present in the precipitate. The data were taken from ref. [1].

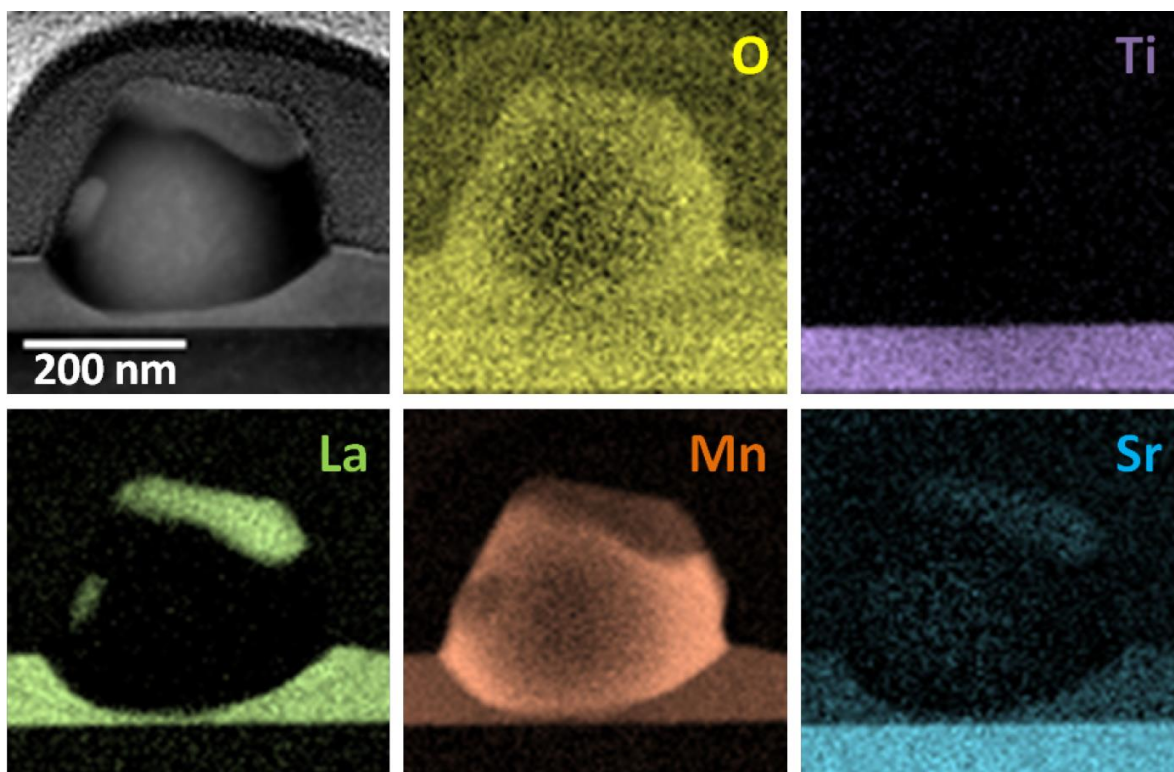


Figure S5. Dark field STEM image showing the LSMO film, the precipitate and the substrate. EELS maps for every involved element reveal the elemental distribution, indicating that the precipitate consists predominantly of Mn and O, while the film and the capping on the precipitate appear to have similar stoichiometries.

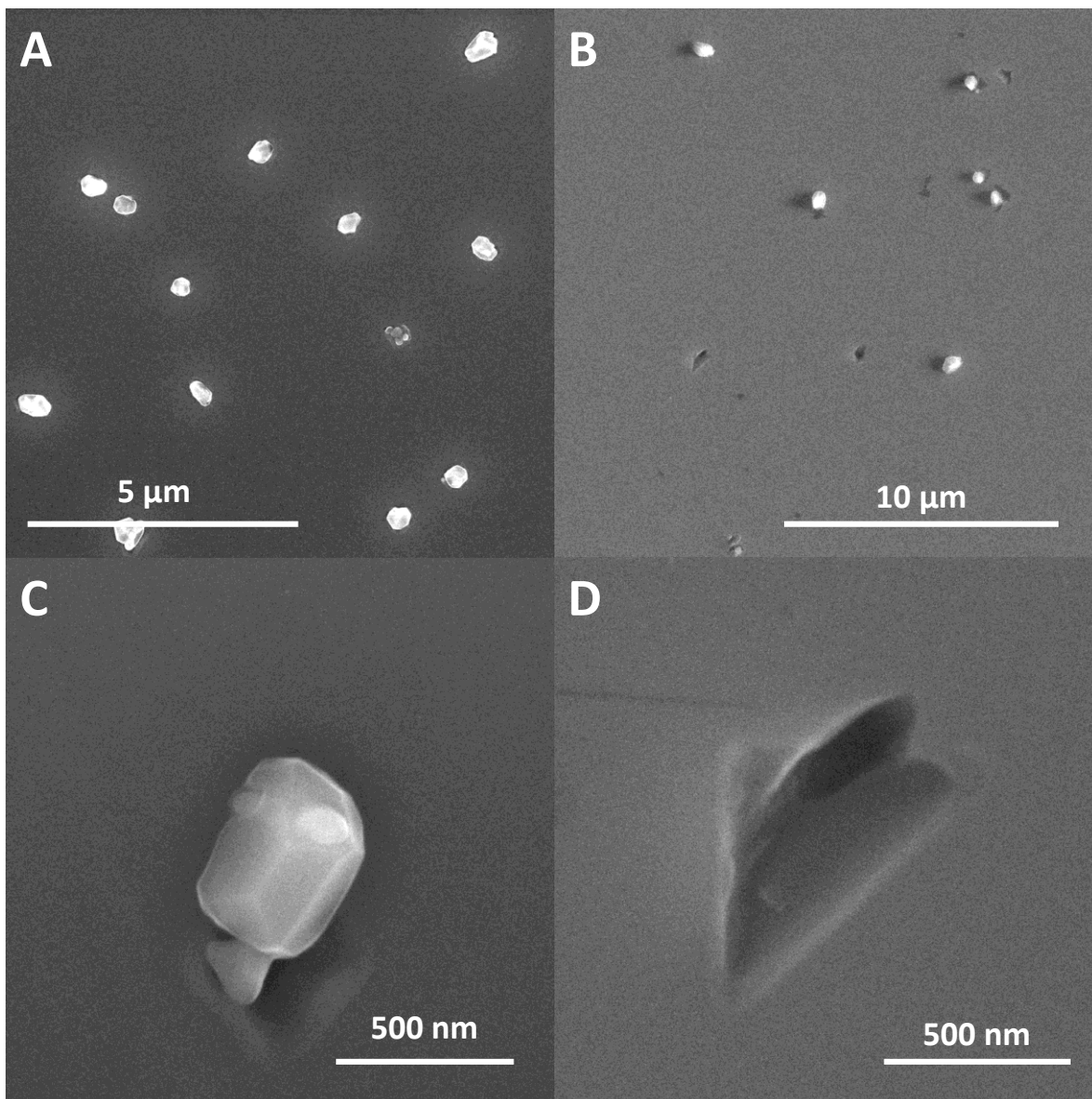


Figure S6. SEM images taken with 15-kV acceleration voltage on Mn-rich LSMO samples. (A) A representative section on a pristine Mn-rich sample with the typical density of Mn₃O₄ precipitates. (B) Large-area scan showing a representative section of a Mn-rich sample after application of the electrochemical measurements. (C) High resolution image on typical Mn₃O₄ precipitate after the electrochemical treatment revealing the preservation of the facets of the precipitate indicating the crystallinity shown by TEM (Figure S4). (D) Example of remaining sink in the LSMO surface where presumably the Mn₃O₄ precipitate was located.

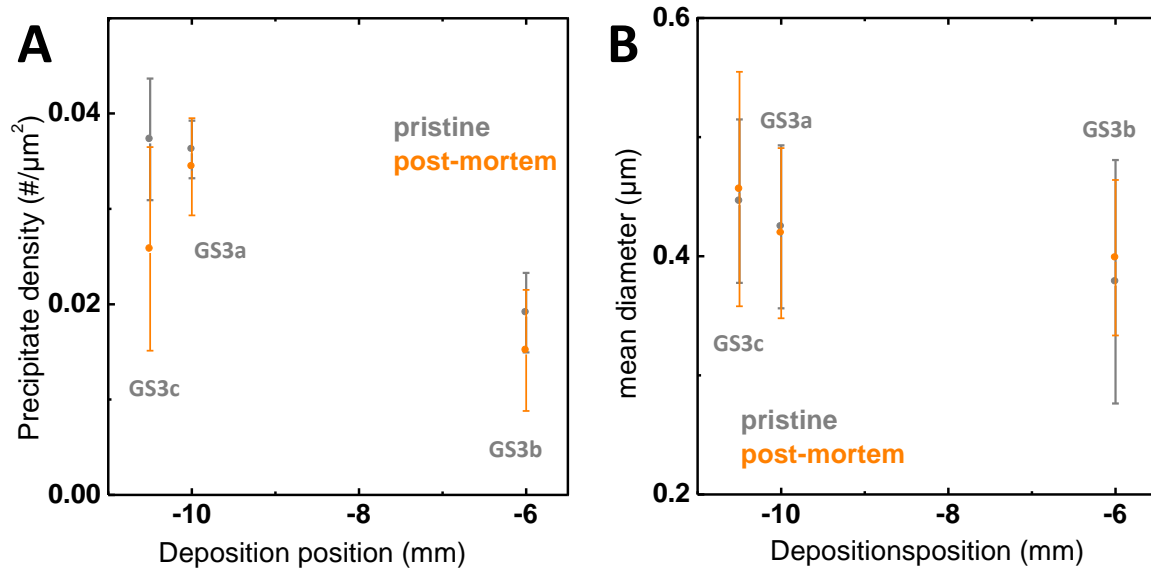


Figure S7. (A) Precipitate density evaluated by imaging the complete surface of the Mn-rich LSMO samples by SEM. The precipitate density was correlated with the deposition position corresponding to a Mn content of + 5.4% in the case of the sample GS3b and +7.2% in the case of the samples GS3a and GS3c. (B) The mean diameter of the Mn_2O_4 precipitates imaged by SEM. The error bars indicate the statistical spread for the complete sample surface in both cases.

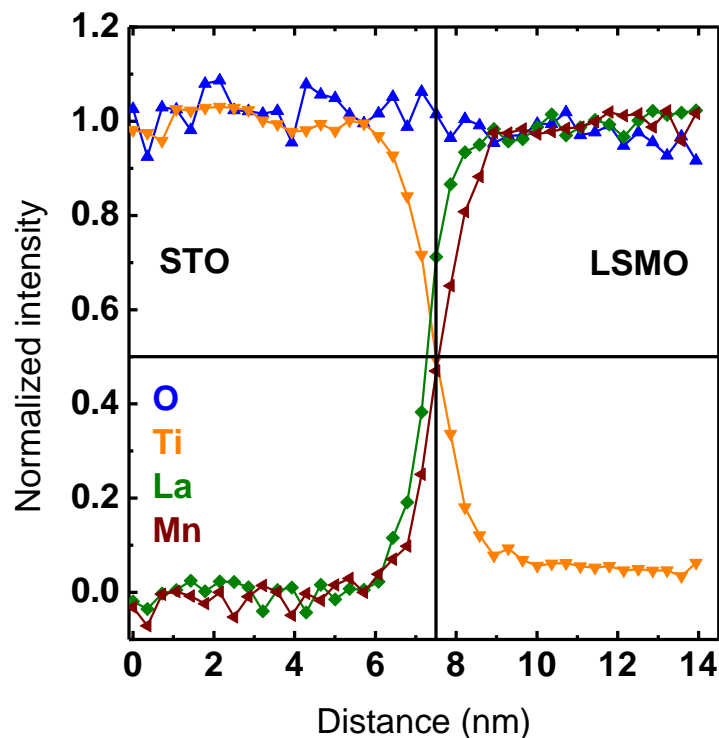


Figure S8. Normalized EELS scans across the interface of a Mn-rich LSMO film on an STNO substrate. The interface is indicated by the black lines based on the error function of a beam with a 1.5-nm dispersion showing the spread of the electron beam. As the point of half intensity for Mn and Ti coincide at the point predicted by the error function, the obtained resolution of the EELS scan has to be close to the dimension of the electron beam.

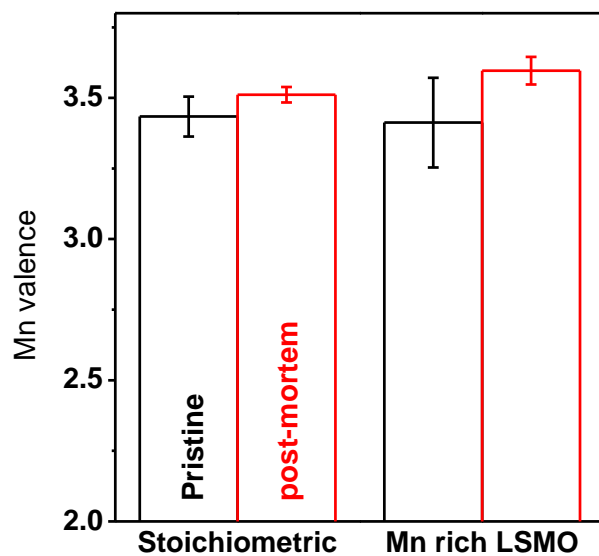


Figure S9. Mn valence states determined by the energy difference between the pre-peak of the O K-edge and the Mn L-edge according to refs. [1,2] for (A) the Mn-rich LSMO and (B) the stoichiometric LSMO comparing the pristine state (black) to the effects of electrochemical treatment (red). The values were determined by averaging the EEL spectra far from the surface in order to obtain bulk values. The indicated error results from the fitting error assuming the accuracy of the energy position to ± 1 eV.

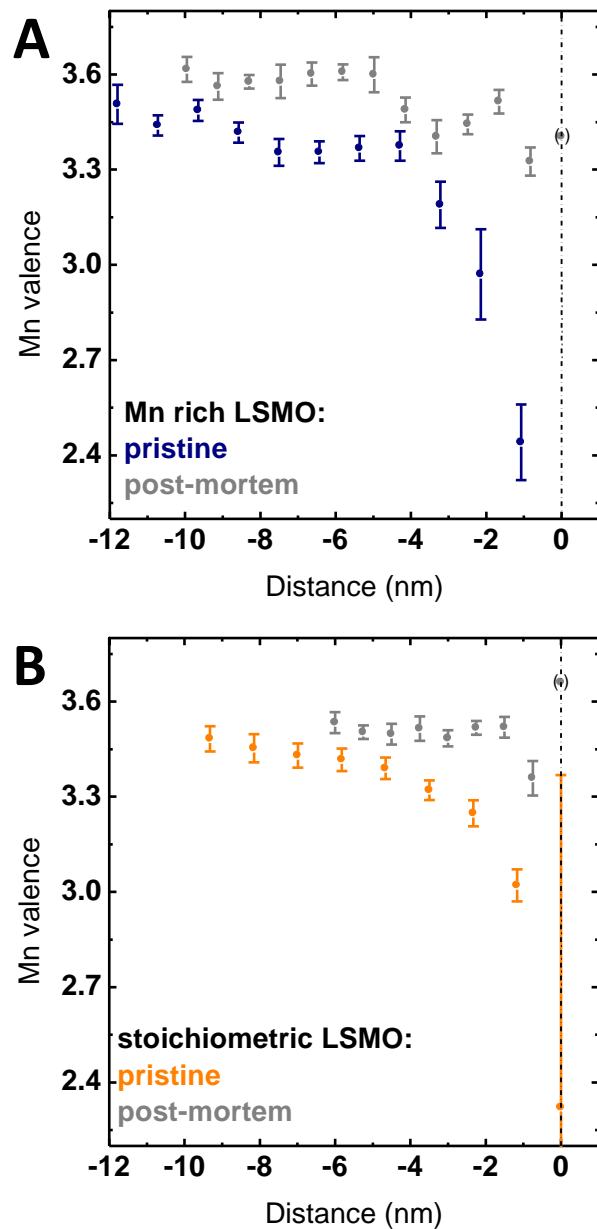


Figure S10. Local variation of Mn valence states determined by the energy difference between the pre-peak of the O K-edge and the Mn L-edge according to refs. [1,2] for (A) the Mn-rich LSMO and (B) the stoichiometric LSMO comparing the pristine state to the effects of electrochemical treatment. The indicated error results from the fitting error assuming the accuracy of the energy position to ± 1 eV. The grey symbols indicate the local distribution of the Mn valence resulting from the electrochemical treatment. The dashed lines indicate the interface between the LSMO film and the electron deposited Pt.

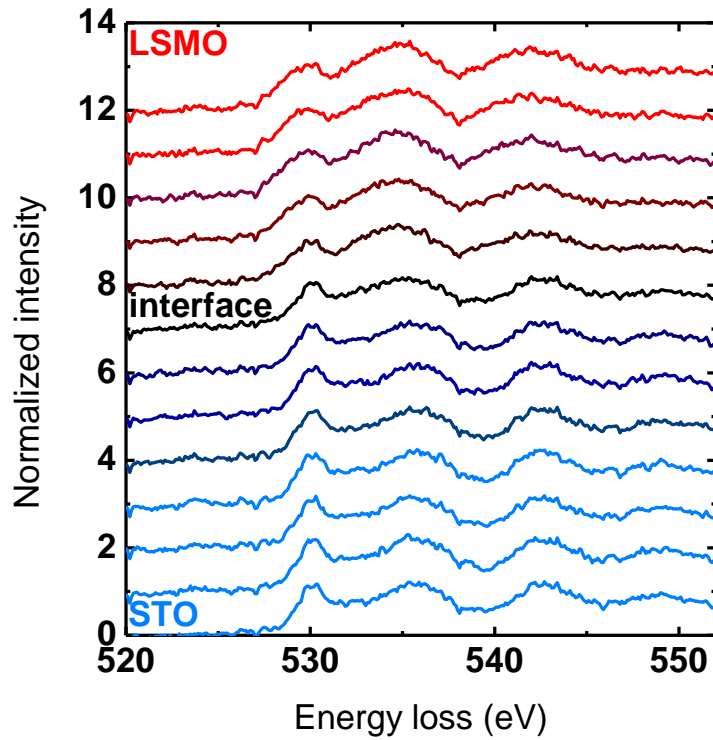


Figure S11. EELS scans at the O K-edge across the interface between a Mn-rich LSMO sample and the STO substrate. The step size of the separation for the spectra was 1.1 nm, resulting in a total mapped spread of 12.9 nm.

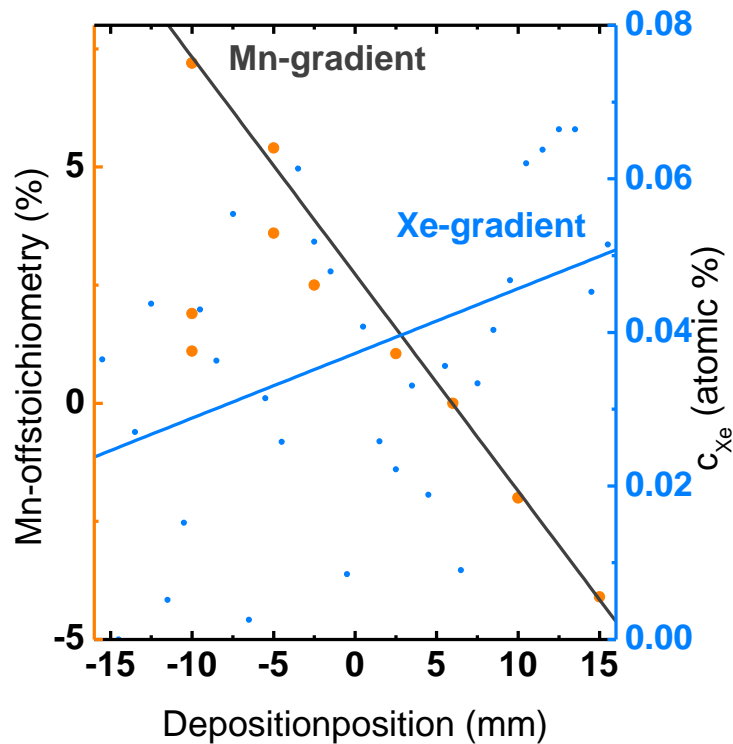


Figure S12. Mn gradient with deposition position resulting from different sputter yields of used elements. Data based on EMP measurements. Xe gradient extracted by EMP measurements as an example for residues of sputter gases present in samples prepared at room temperature.

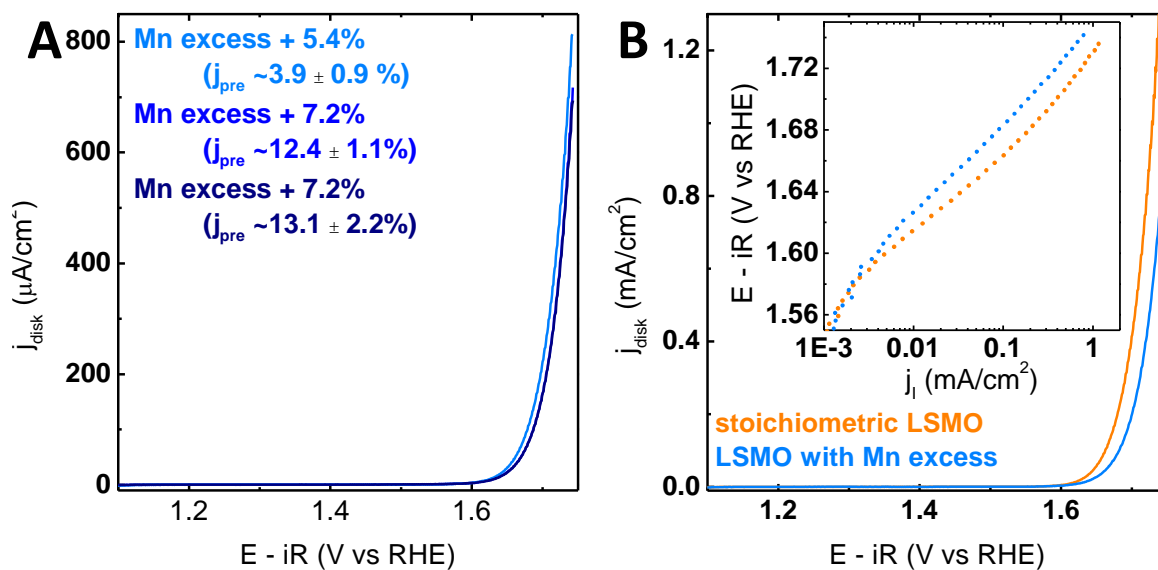


Figure S13. (A) CV measurement of all evaluated Mn-rich LSMO films with the amount of Mn excess shown and indicated by the used color code. (B) Comparison of CV measurements of stoichiometric LSMO and LSMO with Mn excess, but without precipitates. All measurements were performed with Ar-purged 0.1 M KOH supporting electrolyte at 10 mV/s and 1600 rpm. The voltage was corrected for electrolyte resistance ($\sim 47 \Omega$ for all samples). The forward direction of the second cycle is shown.

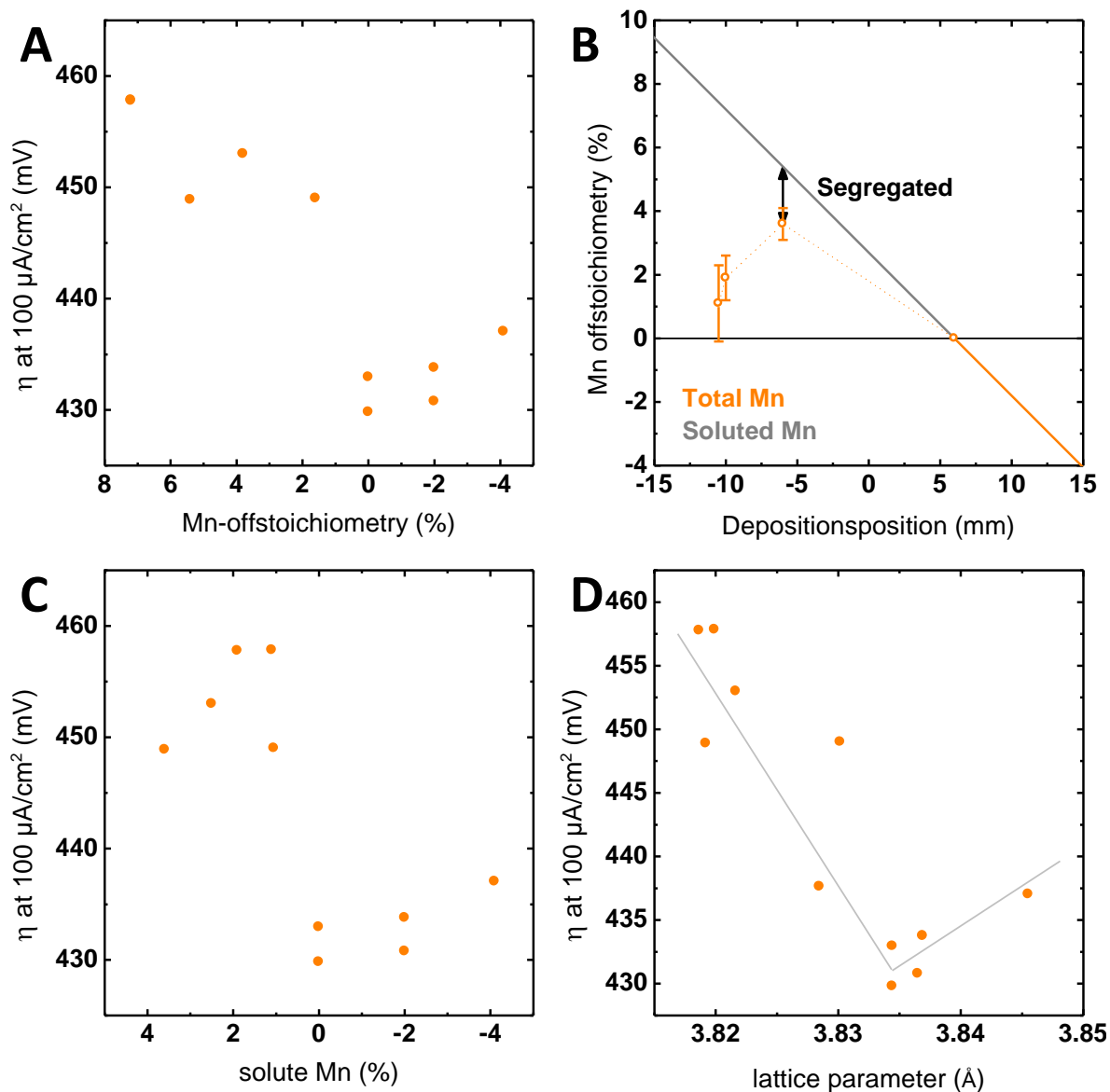


Figure S14. (A) Overpotential η to obtain a current density of 100 $\mu\text{A}/\text{cm}^2$ for all evaluated samples correlated with the Mn off stoichiometry based on the Mn gradient determined by EMP measurements. (B) Correction of the Mn content of the LSMO matrix in the case of the Mn-rich LSMO samples. The correction is based on the density of the Mn_3O_4 precipitates and their total volume estimated by a spherical volume. The total volume of Mn_3O_4 precipitates removes the amount of Mn from the LSMO indicated in (B). (C) Overpotential to obtain a current density of 100 $\mu\text{A}/\text{cm}^2$ for all evaluated samples correlated with the amount of solute Mn in the LSMO film based on the correction shown in (B). (D) Overpotential to obtain a current density of 100 $\mu\text{A}/\text{cm}^2$ for all evaluated samples correlated with the lattice parameter shown in Figure 7A.

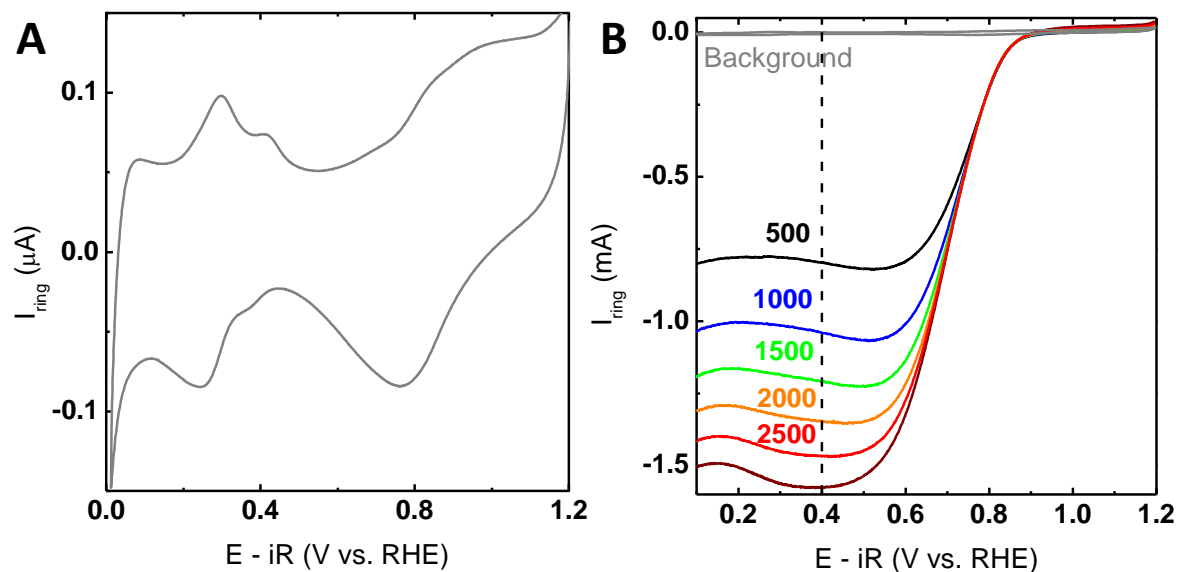


Figure S15. (A) Un-rotated CV measurement of the freshly-polished Pt-ring in Ar saturated 0.1 M KOH supporting electrolyte at 200 mV/s showing the expected features of a polycrystalline Pt metal without surface oxides [3]. (B) Ring currents of a freshly-polished Pt-ring in 0.1 M KOH supporting electrolyte (Ar-purged for the background measurement, O₂-purged for ORR measurements) at 200 mV/s. Rotation speeds were increased from 500–3000 rpm (lines). All measurements shown are the forward direction of the second cycle.

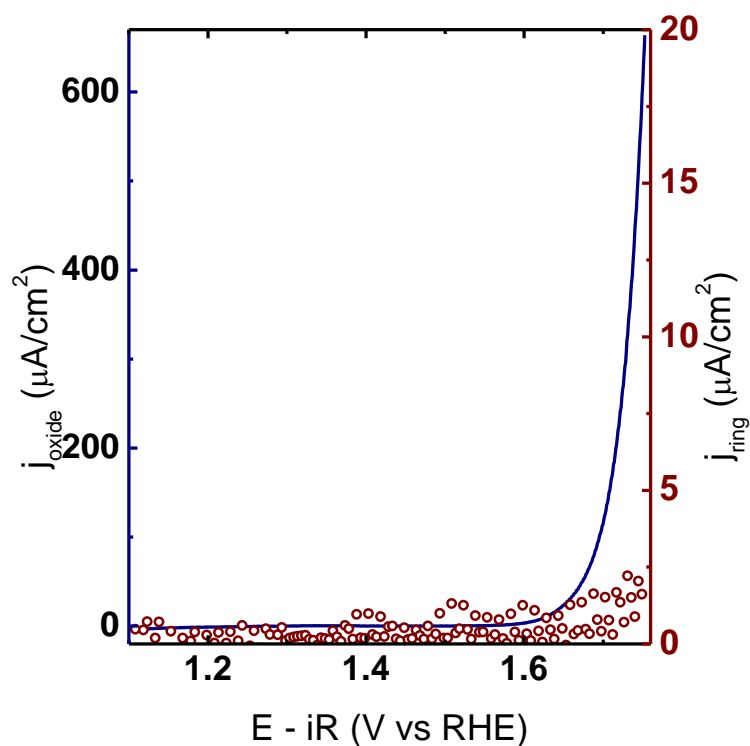


Figure S16. CV measurement of a stoichiometric La_{0.6}Sr_{0.4}MnO₃ film (solid blue line) and the corresponding ring current (open red circles) obtained by CA at 1.2 V vs. RHE to probe for H₂O₂. All measurements were performed with Ar-purged 0.1 M KOH supporting electrolyte at 10 mV/s and 1600 rpm, and the positive-going direction of the second scan is shown.

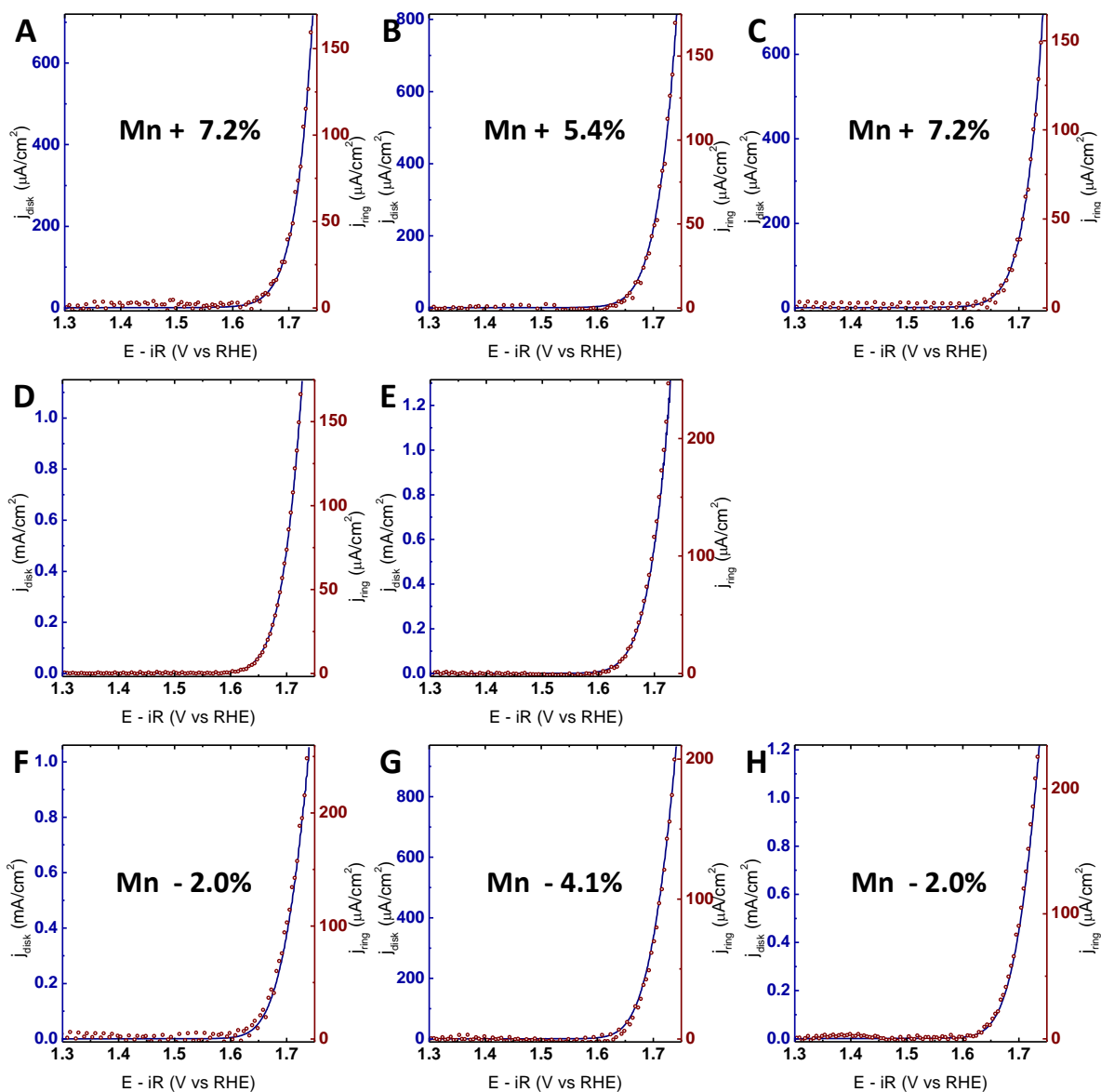


Figure S17. CV measurements of all evaluated $\text{La}_{0.6}\text{Sr}_{0.4}\text{Mn}_{1-x}\text{O}_3$ films (solid blue lines) and the corresponding ring currents (open red circles) obtained by CA at 0.4 V vs. RHE. All measurements were performed with Ar-purged 0.1 M KOH supporting electrolyte at 10 mV/s and 1600 rpm. The voltage was corrected for electrolyte resistance ($\sim 47 \Omega$ for all samples). (A–C) The Mn-rich samples; (D,E) the stoichiometric samples; (F–H) the Mn-deficient LSMO samples. Their respective Mn off-stoichiometry is indicated in each figure.

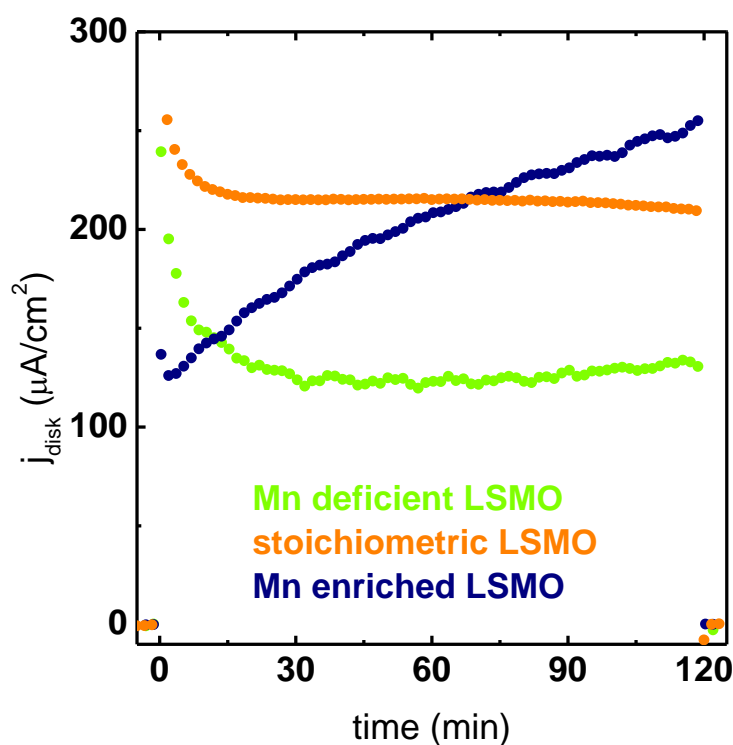


Figure S18. Disk currents of CA measurements for one LSMO of each stoichiometry for 2 h at 1.7 V vs. RHE. Previously and consecutively to the electrolysis, the samples were held at 0.1 V vs. RHE for 10 min. All electrochemical measurements were performed in Ar-saturated 0.1 M KOH and 1600 rpm. The measurement protocol applied to the samples prior to electrolysis/extensive CV measurements was identical for all samples.

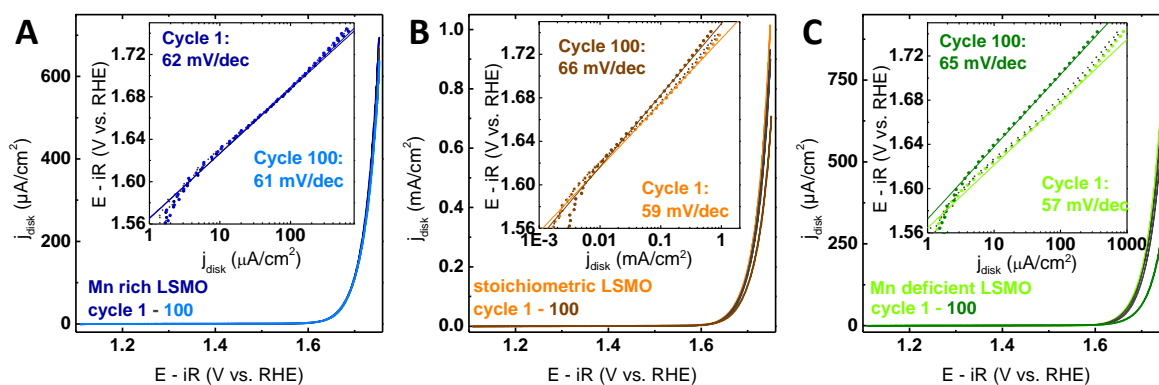


Figure S19. Comparison of CV measurements made prior to the applied long-term measurement and subsequent to the long-term measurement. Representative CV measurements are shown for all evaluated stoichiometries. All measurements were performed with Ar-purged 0.1 M KOH supporting electrolyte at 10 mV/s and 1600 rpm. The voltage was corrected for electrolyte resistance ($\sim 47 \Omega$ for all samples). The forward direction of the second cycle is shown. The inset shows the Tafel analysis comparing the CV before and after the long-term measurement with the determined Tafel slope stated. (A–C) The comparison of the effects extensive cycling comparing the first cycle and the 100th cycle of each sample.

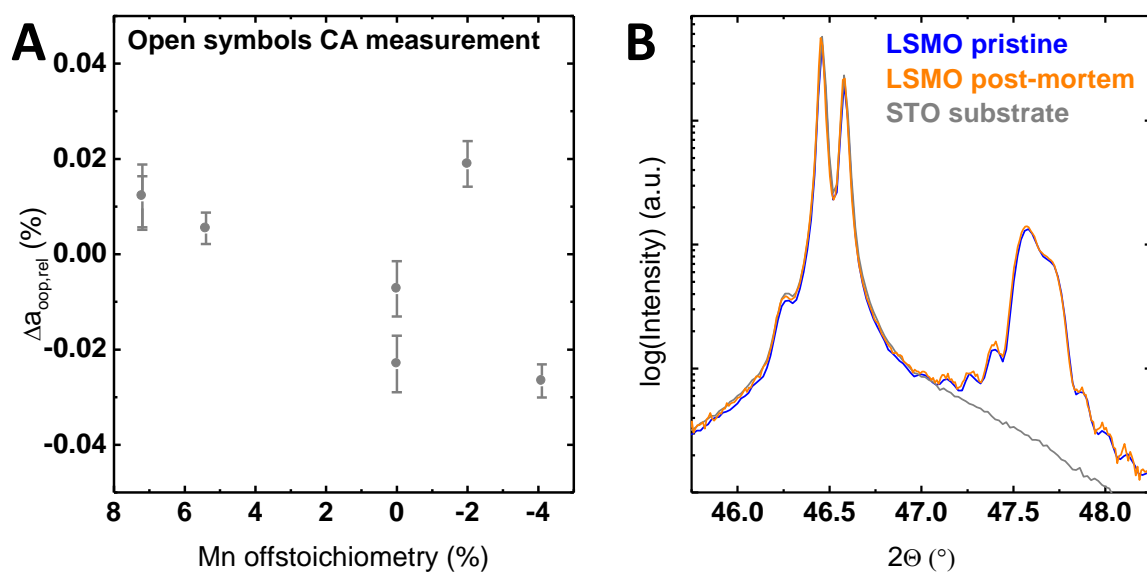


Figure S20. (A) Relative changes in the lattice parameters of the initial samples and after the electrochemical measurements based on wide angle out-of-plane X-ray diffraction spectra using a monochromator. (B) A detailed 2θ XRD scan at the 200 LSMO reflex comparing the blank substrate and a Mn-rich LSMO film prior to electrochemical measurements and directly after the applied electrochemical measurement (in this case, extensive cycling).

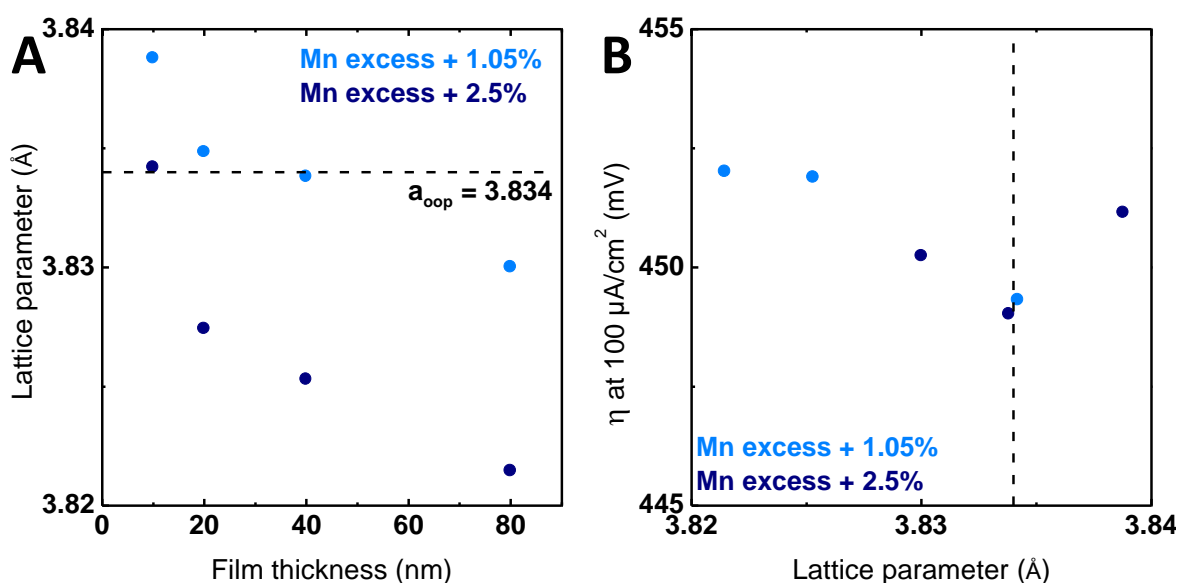


Figure S21. (A) Thickness decency of lattice parameters based on the sample series reported in ref. [4] for LSMO with small Mn excess. (B) Overpotential required to obtain $100 \mu\text{A}/\text{cm}^2$ in dependence of the lattice parameter for two offstoichiometries analogous to Figure 6B. The dashed line corresponds to the lattice parameter with the highest activity, as can be seen in Figure 6B.

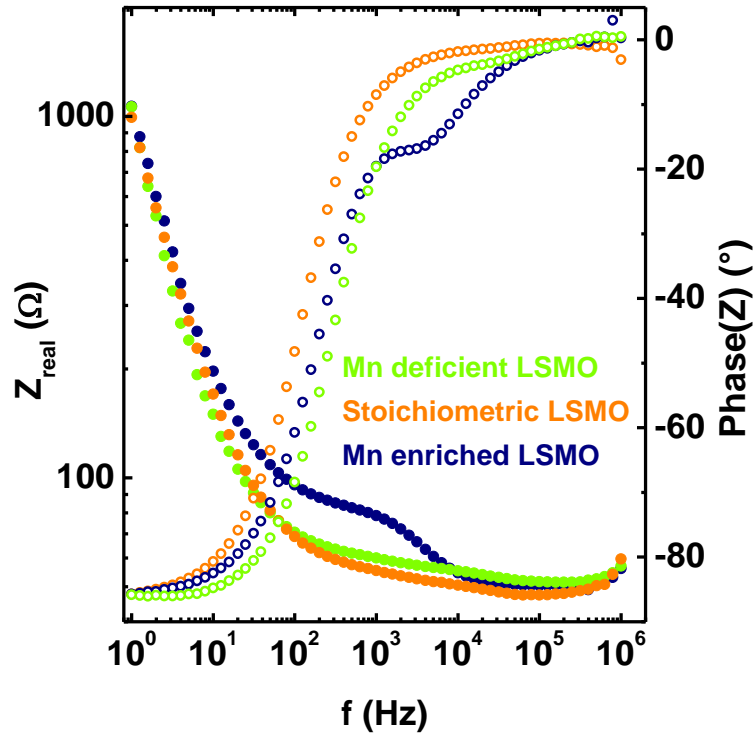


Figure S22. Electrochemical impedance spectroscopy (EIS) exemplarily shown for each stoichiometry. The EIS was conducted with an amplitude of 10 mV/s at open circuit potential and used to determine the uncompensated electrolyte resistance by the high frequency intercept. The additional feature for Mn-rich LSMO can be attributed to the additional interface due to the Mn_2O_4 precipitates.

Table S1. Analysis of surface roughness based on AFM images on all samples. The roughness factor is the ratio between the surface area and the projected area.

Sample	RMS (nm)	Roughness factor
Mn deficient	0.16 ± 0.04	1.000 ± 0.000
Mn rich (800 °C deposition temp.)	17.75 ± 4.29	1.006 ± 0.001
Stoichiometric LSMO	0.12 ± 0.03	1.000 ± 0.000

Table S2. Voltages of select highly active electrocatalysts for the OER at 100 $\mu\text{A}/\text{cm}^2_{\text{ox}}$ in 0.1 M KOH.

Material	E (V vs. RHE)*	Conditions	Reference
$\text{La}_{0.6}\text{Sr}_{0.4}\text{MnO}_3$	1.66	Epitaxial thin film on 0.5 wt% Nb:SrTiO ₃	This work
$\text{La}_{0.8}\text{Sr}_{0.2}\text{MnO}_3$	1.695	Epitaxial thin film on 0.5 wt% Nb:SrTiO ₃	[5]
$\text{La}_{0.8}\text{Sr}_{0.2}\text{MnO}_3$	1.68	Polycrystalline film on Pt	[6]
$\text{Ba}_{0.5}\text{Sr}_{0.5}\text{Co}_{0.8}\text{Fe}_{0.2}\text{O}_3$	1.525	Epitaxial thin film on $\text{La}_{0.8}\text{Sr}_{0.2}\text{MnO}_3$	[5]
RuO_2 (100)	1.516	Epitaxial thin film on MgO	[7]
RuO_2 (110)	1.547	Epitaxial thin film on MgO	[7]
IrO_2 (100)	1.62	Epitaxial thin film on SrTiO ₃	[7]
IrO_2 (110)	1.689	Epitaxial thin film on SrTiO ₃	[7]
SrIrO_3	1.548	Epitaxial thin film on DyScO ₃	[8]
LaCoO_3	1.592	Epitaxial thin film on Nb:SrTiO ₃	[9]
RuO_2	1.568 ¹	Nanoparticle on GC	[10]
IrO_2	1.582 ¹	Nanoparticle on GC	[10]
LaMnO_3	1.682	Nanoparticle on GC	[9]
$\text{Ba}_6\text{Mn}_5\text{O}_{16}$	1.664	Nanoparticle on GC	[11]
Co_3O_4	1.612	Nanoparticle on GC	[11]
LaCoO_3	1.583	Nanoparticle on GC	[11]
$\text{La}_{0.4}\text{Sr}_{0.6}\text{CoO}_3$	1.564	Nanoparticle on GC	[11]
$\text{La}_{0.8}\text{Sr}_{0.2}\text{MnO}_3$	1.771	Nanoparticle on GC	[5]
$\text{La}_{0.6}\text{Sr}_{0.4}\text{MnO}_3$	1.97 ²	Pellet	[12,13]

¹ Data extrapolated using <http://arohatgi.info/WebPlotDigitizer>.

² Using the roughness factor of 1200, 100 $\mu\text{A}/\text{cm}^2_{\text{ox}}$ equals 0.12 $\text{A}/\text{cm}^2_{\text{pellet}}$. The voltage was calculated by extrapolation using the Tafel equation with a Tafel slope of 125 mV/dec and exchange current density of 1.4×10^{-7} $\text{A}/\text{cm}^2_{\text{pellet}}$.

Table S3. List of all measured samples with their initial thickness and the relative changes after employing the electrochemical measurements based on fitted XRR spectra.

sample	Mn off-stoichiometry (%)	film thickness (nm)	Change in thickness (nm)
GS2a	-2	75.8	-0.17
GS2b	-4.1	76.3	-0.33
GS2c	-2	75.3	-0.28
GS3a	7.2	76.5	0.13
GS3b	5.4	82.5	-0.2
GS3c	7.2	77.1	-1.74
GS6a	0	72.4	-0.51
GS6b	0	76.9	-0.31

References:

1. Paterson, J. H.; Krivanek, O. L. ELNES of 3d transition-metal oxides. *Ultramicroscopy* **1990**, *32*, 319–325.
2. Rask, J. H.; Miner, B. A.; Buseck, P. R. Determination of manganese oxidation states in solids by electron energy-loss spectroscopy. *Ultramicroscopy* **1987**, *21*, 321–326.
3. Sheng, W.; Gasteiger, H. A.; Shao-Horn, Y. Hydrogen Oxidation and Evolution Reaction Kinetics on Platinum: Acid vs Alkaline Electrolytes. *J. Electrochem. Soc.* **2010**, *157*, B1529.
4. Scholz, J.; Risch, M.; Stoerzinger, K. A.; Wartner, G.; Shao-Horn, Y.; Jooss, C. Rotating Ring–Disk Electrode Study of Oxygen Evolution at a Perovskite Surface: Correlating Activity to Manganese Concentration. *J. Phys. Chem. C* **2016**, *120*, 27746–27756.
5. Risch, M.; Stoerzinger, K. A.; Maruyama, S.; Hong, W. T.; Takeuchi, I.; Shao-Horn, Y. $\text{La}_{0.8}\text{Sr}_{0.2}\text{MnO}_{3-\delta}$ Decorated with $\text{Ba}_{0.5}\text{Sr}_{0.5}\text{Co}_{0.8}\text{Fe}_{0.2}\text{O}_{3-\delta}$: A Bifunctional Surface for Oxygen Electrocatalysis with Enhanced Stability and Activity. *J. Am. Chem. Soc.* **2014**, *136*, 5229–5232.
6. Miyahara, Y.; Miyazaki, K.; Fukutsuka, T.; Abe, T. Catalytic Roles of Perovskite Oxides in Electrochemical Oxygen Reactions in Alkaline Media. *J. Electrochem. Soc.* **2014**, *161*, F694–F697.
7. Stoerzinger, K. A.; Qiao, L.; Biegalski, M. D.; Shao-Horn, Y. Orientation-Dependent Oxygen Evolution Activities of Rutile IrO_2 and RuO_2 . *J. Phys. Chem. Lett.* **2014**, *5*, 1636–1641.
8. Tang, R.; Nie, Y.; Kawasaki, J. K.; Kuo, D.; Petretto, G.; Rignanesi, G.; Shen, K. M.; Schlom, D. G.; Suntivich, J. Oxygen evolution reaction electrocatalysis on SrIrO_3 grown using molecular beam epitaxy. *J. Mater. Chem. A* **2016**.
9. Hong, W. T.; Risch, M.; Stoerzinger, K. A.; Grimaud, A.; Suntivich, J.; Shao-Horn, Y. Toward the rational design of non-precious transition metal oxides for oxygen electrocatalysis. *Energy Environ. Sci.* **2015**, *8*, 1404–1427.
10. Lee, Y.; Suntivich, J.; May, K. J.; Perry, E. E.; Shao-Horn, Y. Synthesis and Activities of Rutile IrO_2 and RuO_2 Nanoparticles for Oxygen Evolution in Acid and Alkaline Solutions. *J. Phys. Chem. Lett.* **2012**, *3*, 399–404.
11. Grimaud, A.; Carlton, C. E.; Risch, M.; Hong, W. T.; May, K. J.; Shao-Horn, Y. Oxygen Evolution Activity and Stability of $\text{Ba}_6\text{Mn}_5\text{O}_{16}$, $\text{Sr}_4\text{Mn}_2\text{CoO}_9$, and $\text{Sr}_6\text{Co}_5\text{O}_{15}$: The Influence of Transition Metal Coordination. *J. Phys. Chem. C* **2013**, *117*, 25926–25932.
12. Matsumoto, Y.; Sato, E. Oxygen evolution on $\text{La}_{1-x}\text{Sr}_x\text{MnO}_3$ electrodes in alkaline solutions. *Electrochim. Acta* **1979**, *24*, 421–423.
13. Bockris, J. O.; Otagawa, T. Mechanism of oxygen evolution on perovskites. *J. Phys. Chem.* **1983**, *87*, 2960–2971.